COVALENT EFFECTS IN MOLECULE–SURFACE CHARGE EXCHANGE: O₂ ON Ag(111)

Marjanne C. ZONNEVYLLE *, Roald HOFFMANN

Department of Chemistry and Materials Science Center, Cornell University, Ithaca, NY 14853, USA

Paul J. VAN DEN HOEK **

*FOM-Institute for Atomic and Molecular Physics, Kruislaan 407, 1098 SJ Amsterdam,
The Netherlands*

and

Rutger A. VAN SANTEN

*Laboratory of Inorganic Chemistry and Catalysis, Technical University of Eindhoven, P.O. Box 513,
5600 MB Eindhoven, The Netherlands*

The formation of negatively charged ions (O_2^-, O^-) in the scattering of oxygen from silver surfaces is difficult to explain in the Brako–Newns scheme. To understand these processes, we have performed extended Hückel tight binding calculations on model Ag(111) slabs, placing O_2 adsorbates at various sites and molecular orientations. As the survival probability of a negatively charged ion *leaving* the surface is determined by the back-tunneling frequency, the molecular ion survival probability should increase as the O_2–Ag interaction decreases, and vice versa. On the other hand, the dissociation probability will increase with increasing interaction strength. The strength of the O_2–Ag interaction can be gauged by the dispersion found in the projected DOS of the O_2 affinity level $1\pi_g$. The second moment serves as a measure of relative dispersion, and in addition, can be related to the tunneling frequency. We find that bridging and hollow sites have the strongest O_2–Ag interaction, thus the lowest survival probability of negative ions and the highest degree of dissociation. The interaction at top sites is much less. These results can be used to explain the higher $O^-/(O^- + O_2^-)$ ratio observed at more grazing incident beam angles.

1. Introduction

Negative ion formation in scattering of atoms and molecules from metal surfaces is frequently observed [1]. Brako and Newns have formulated a useful

* Current address: Koninklijke/Shell-Laboratorium, Amsterdam, P.O. Box 3003, 1003 AA Amsterdam, The Netherlands.
** Current address: Koninklijke/Shell Exploratie en Productie Laboratorium, P.O. Box 60, 2280 AB Rijswijk, The Netherlands.

description of such processes [2,3]. As the incoming molecule (or atom) approaches the surface, the affinity level (energy ϵ_a) falls in energy due to Coulombic interaction with its image potential. At some distance r, typically ~ 5 Å, the affinity level crosses the Fermi level, ϵ_F. Electrons can then tunnel from the surface to the molecule, so that it becomes negatively charged. Since the molecule is now very close to the surface, the interaction with the surface is very strong, and this tunneling frequency is very high, with the result that the affinity level becomes completely filled. After the scattering event, the molecule moves away from the surface, and it can return this charge to the surface when ϵ_a has risen above ϵ_F. Since this occurs at larger distances from the surface, the interaction, and therefore the back-tunneling frequency, is much lower. Thus the final charge state of the exiting molecule is determined by the survival probability of the negative ion. When the interaction with the surface is relatively strong, the survival probability will be relatively low, whereas when the interaction is weak, the survival probability is high.

Under certain simplifying conditions, Brako and Newns deduce that the fraction of surviving negative ion f is given by:

$$f = \exp\left(-2\Delta_a^0/\alpha v\right), \tag{1}$$

where Δ_a^0 is the width of the affinity level as it crosses ϵ_F, α is the time constant describing the exponential form of Δ_a, and v is the normal component of the velocity. This formula qualitatively reflects the survival probability in non-adiabatic charge transfer. A strong interaction (large Δ_a^0) gives a small negative ion fraction, and a large perpendicular escape velocity v gives a large fraction, as the charge has little time to tunnel back.

For molecules, the situation becomes more complex. It has been pointed out that symmetry (e.g., the orientation of the molecular axis) can play a role in the interaction with the surface by affecting the evolution of Δ_a. For diatomic molecules, this interaction will weaken the interatomic bond, thereby increasing the dissociation probability of the molecule. It should be pointed out, therefore, that a strong molecule–surface interaction, i.e. a large broadening of Δ_a, leads to a *high* dissociation probability, but on the contrary to a *low* survival probability of negative molecular ions. We will return to this point later.

Although the Brake–Newns model explains charge transfer from metal surfaces, charge exchange on non-metals, for example, Si(100) [4] and graphite [5], has recently been observed. An explanation based on charge exchange has been proposed [6] for the vibrational excitation of I_2 scattered from insulator surfaces [7]. Negative ion formation has also been observed by Kleyn and coworkers in O_2 scattering from Ag(111) [8,9a]. They have focused on grazing incidence, medium energy (10–300 eV) scattering of O_2^+ beams in this energy region. It is assumed that the beam will (partially) neutralize upon approach to

the surface. Intensity distribution plots of scattering angle versus energy indicate formation of both O_2^- and O^-, as well as neutral O and O_2.

Although silver is a metal, the Brako–Newns model cannot be applied in this case either. The electron affinity of O_2 is too low (0.5 eV) so as to allow the image potential to lower the affinity level below the Ag Fermi level (work function = 4.5 eV). In this work, we propose that *covalent*, i.e. "chemical", interactions between atom or molecule and surface can be responsible for the charge exchange, and that the affinity level need not cross ϵ_F. This is eplained by the fact that particle–surface interactions can force a considerable part of the affinity level DOS below ϵ_F. We have performed a series of extended Hückel (EH) tight-binding calculations [10] to better understand the O_2–Ag(111) interactions at a variety of sites. Our aim is to describe these interactions using a group orbital analysis, and to compare their strengths by considering the dispersion induced in the O_2 molecular levels. Although the EH calculation method is most certainly *not* quantitative in nature, a number of different "yardsticks" can be constructed for measuring interaction strengths by means of the relative degree of dispersion. The statistically most precise method is to calculate the second moment of the O_2 levels. The second moment, in turn, can be mathematically related to the transition probability of and electron tuneling from substrate to surface (or vice versa). The results will be used to explain the observed formation of charge transfer as well as dissociation products.

Our discussion will begin with a consideration of various computational parameters and details, followed by a brief discussion concerning the contruction of group orbitals and their utility in surface–adsorbate analysis. The O_2–Ag interaction is then analyzed at a number of important sites and geometries. The relative interaction strength is determined from the O_2 projected DOS by a variety of techniques, the most important being calculation of the second moment. This section also contains a derivation of the mathematical relationship between the second moment and the tunneling probability. Finally, the experimental results are reconsidered in terms of the present analysis.

2. Method

A three layer slab of Ag(111) was chosen to model the substrate; this number has previously been shown to be a fair compromise between slab thickness and computational economy [11]. The O_2 coverage was set to 1/4 on one side of the slab so as to reduce to a minimum interadsorbate interactions. The precise coordination mode to the Ag(111) surface should certainly influence the course of the subsequent reaction. Three high-symmetry sites are available to an adsorbate on the hexagonal surface: on-top, bridging and
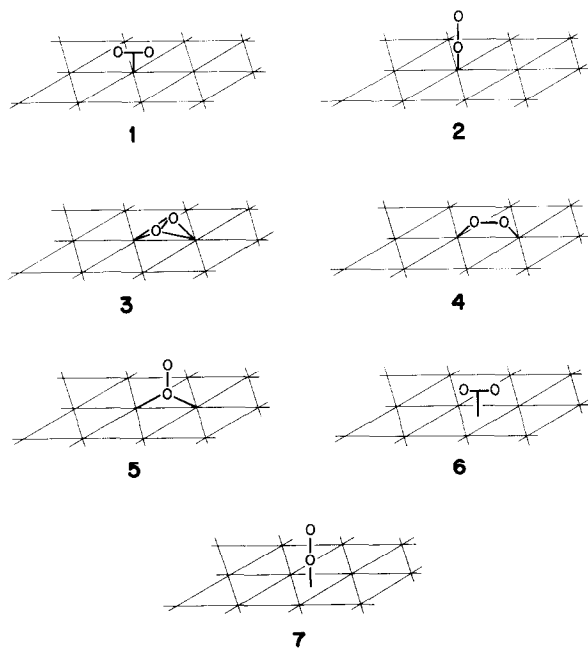
Schemes 1–7.

three-fold hollow. At each of these, O_2 orientations both parallel and perpendicular to the surface should be considered. Two bridging parallel geometries can be envisaged – the O_2 axis can be placed either perpendicular (labeled "bridging parallel") or parallel (labeled "di-σ") to the Ag–Ag bond. There are two types of three-fold hollow positions on the Ag(111) surface; half are directly above an atom in the second layer, the other half above one in the third layer. As the Ag–Ag distance is so long (2.889 Å) in comparison to the O–O (1.2 Å) and Ag–O (see continuation) distances, the two types should give very similar results, and we choose the hollow above a second layer Ag atom. The seven resulting models are shown in schemes 1–7.

Two problems remain in defining these models: the choice of oxygen and silver parameters and the Ag–O separation distance. According to classical trajectory calculations, the center-of-mass turning point is found to be between 1.0 and 1.8 Å outside of the surface [12,13], thus short Ag–O distances must certainly be considered. In addition, to probe the outward range of the Ag–O interaction, longer distance should be sampled as well. Three distances were chosen: 1.6, 2.0 and 2.5 Å. Calculations were performed on all seven models at the two shorter distances, and on the parallel on-top as in scheme 1 at 2.5 Å as well. As a negligible Ag–O interaction was observed for the latter geometry based on the complete lack of dispersion of the O_2 projected density

$3\sigma_u$ —

$1\pi_g$

8

$3\sigma_g$
$1\pi_u$
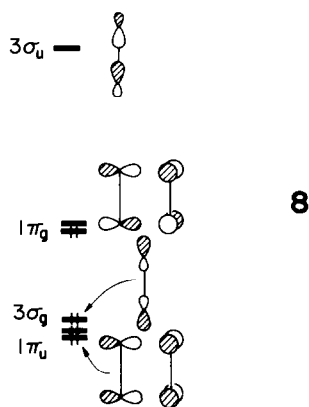
Scheme 8.

of states (DOS), no further calculations were performed at this long separation distance. However, this finding does not in any way eliminate the possibility of Ag–O interactions in the real systems at similar distances.

Silver parameters were chosen which produced a Fermi energy (-8.47 eV) in line with calculations on neighboring metals (Cu: -7.58 eV [14a], Au: -10.61 eV [14b], Ni: -8.58 eV [14c], Pd: -9.43 eV [14d] and Pt: -10.10 eV [14a]) as well as an energy difference of ~ 5.0 eV between ϵ_F and the center of the Ag d band. This value is found by He II UPS on Ag(111) [15], KKR calculations [16] and previous EH cluster calculations [17]. These parameters were produced by shifting the Ag 5s and Ag 5p levels down from -7.71 and -3.83 to -9.00 and -5.00 eV respectively, and retaining the Ag d H_{ii} of -13.50 eV [18].

Typical oxygen parameters [#1] place the half occupied O_2 $1\pi_g$ level 4.5 eV below the calculated ϵ_F of Ag. The frontier orbitals of O_2 are shown in scheme 8. Because the degenerate $1\pi_g$ molecular level is half-occupied in free, neutral O_2, retaining this low value will result in the indiscriminate transfer of two electrons from the substrate to the molecule, regardless of site, adsorption geometry or Ag–O separation distance. As our aim is to distinguish between the sites, and find those which provide the strongest Ag–O_2 interaction, this choice will not prove useful. Instead, we perform a charge iteration on oxygen [19] as an O_2 adsorbate in scheme 1 at both 1.6 and 2.0 Å, and in the bulk Ag_2O structure. The latter may serve as a model for the subsurface oxygen which may exist under certain conditions on silver surface [20]. The results for the three calculations agree to within 0.3 eV, and we arrive at the new H_{ii} of -26.7 and -10.1 eV for 2s and 2p respectively. Now the O_2 $1\pi_g$ level is only 0.4 eV below the Ag ϵ_F.

[#1] Typical O 2s $H_{ii} = -32.3$ eV, O 2p $H_{ii} = -14.8$ eV.

Although we should now be able to distinguish between the electronic characteristics of the various O_2 sites on Ag(111), the Ag d band in the Ag_2O DOS incorrectly falls *below* the O p band, contrary to HFS cluster calculations [21] and contrary to electronegativity arguments. The question arises as to whether the chemical environment of oxygen in Ag_2O and subsurface oxygen in silver metal is in fact similar. We would expect them to be dissimilar; for one, Ag_2O is an insulator whereas subsurface oxygen is metallic. Also consider the fact that the Madelung energy is not included in these calculations: this correction accounts for the interaction of any one electron with the electrostatic field arising from the nonzero net charges on surrounding atoms. In Ag_2O, the charge separation will be quite strong, thus this term will be large as well. The incorporation of the correction should drive the oxygen levels below the Ag d band. However, in the case of subsurface oxygen, the concentration of oxygen will be so low that very little charge localization is to be expected. The Coulomb interaction will be smaller, and the Madelung correction less. The result is that the O p levels will rise up, and our choice of the higher lying O parameters can be justified. This is, in fact, observed with HFS cluster calculations of oxygen adsorption onto silver surfaces [9b,9c].

3. Group orbitals

As we will be using the concept of group orbitals as developed by van Santen [22] to analyze the results of the seven Ag(111)–O_2 models, a brief description is in order to highlight their usefulness in describing substrate–adsorbate interactions in general. Group orbitals are the linear combinations of the pure, unmixed atomic orbitals on a group of atoms. These are *not* the fragment molecular orbitals (FMO's) of the group of atoms, since FMO's allow for mixing between different atomic orbitals. If we consider a group of two carbon atoms, for example, then the two group orbitals resulting from the s atomic orbitals are {s + s} and {s − s}, scheme 9. The related σ and σ^* FMO's will have some p character mixed in, scheme 10, or d character if carbon is replaced by a transition metal.
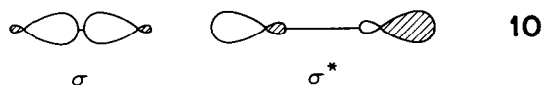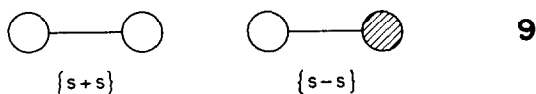
Schemes 9 and 10.

If group orbitals, instead of atomic orbitals, are used to form a basis set, the group orbitals can be used to classify and separate crystal orbitals. From simple band theory, we know that the bonding combinations of a set of crystal orbitals derived from some particular atomic orbital will generally lie at a lower energy than the non-bonding or antibonding combinations. The projected DOS of that atomic orbital will pick up all of these states, whereas the projected DOS of a bonding group orbital will preferentially select the mainly bonding crystal orbitals at lower energies, and an antibonding group orbital will select the mainly antibonding crystal orbitals at higher energies. The projected DOS of group orbitals (GODOS) can thus be used to localize interactions directly, whereas atomic orbitals projections can usually serve only as an indirect guide. The normalization is the same as for atomic orbitals, i.e.:

$$\int \rho_{GO}(E)\, dE = \int \rho_{AO}(E)\, dE = 1. \tag{2}$$

Consider the example of a bare three-layer slab of Ag(111). As the d orbitals are very contracted, the differentiation established by group orbitals will be difficult to see. Instead we choose the very diffuse and strongly interacting Ag s orbitals. Depicted in the left panel of fig. 1 is the magnified projected DOS of an s orbital in the surface layer, the dark solid line, as well as the projections of a number of group orbitals. The four integration curves corresponding to each of the projections is found in the righthand panel. Two simple units, the Ag–Ag dimer, and the triangular Ag_3, form the basis for the group orbitals. The projection of the Ag_2 bonding combination is shown as a dotted line, and a thin solid line is used for the antibonding combination. More s–s bonding states than antibonding states appear at low energies, below ϵ_F, while antibonding states predominate above ϵ_F. It can be verified graphically that the sum of the $\{s + s\}$ and $\{s - s\}$ GODOS add to twice the s atomic orbital projection, and that, at any point in energy, the s atomic orbital integration is the average of the two group orbital integration. The bonding Ag_3 group orbital is drawn as a dashed line; the projection of the degenerate antibonding pair is equivalent to the Ag_2 antibonding one, thus the thin solid line. The Ag_3 bonding combinations are even more strongly localized in the low energy regions than those of Ag_2. Note also that the median energy, the energy equivalent to 50% filling, is ~ 1.0 eV lower for the Ag_3 bonding group orbital than for the Ag_2 set. Requiring bonding between three neighboring atoms rather than two is a stronger restriction on the crystal orbitals, one that few at higher energies can meet.

Let us now use these concepts to dissect the $Ag-O_2$ interaction in the perpendicular bridging of scheme 5, $d(Ag-O) = 1.6$ Å. The problem is to identify which particular metal orbitals are involved with which O_2 MO's. Because of their orientation, we expect the crystal orbitals resulting from the
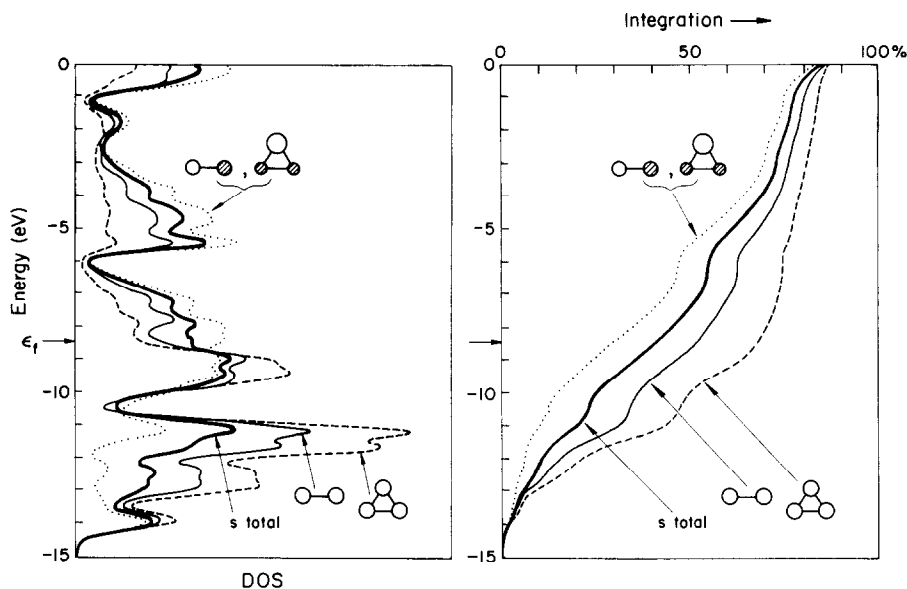
Fig. 1. Example of group orbital projected DOS and GODOS in left panel, and corresponding integration curves in right panel for surface Ag s orbital in bare Ag(111) slab. The dark solid line is the total surface s atomic orbital projection. The Ag$_2$ group orbitals are {s+s}, dotted, and {s−s}, thin solid line. The triangular Ag$_3$ group orbitals are {s+s+s}, dashed, and the degenerate set {2s−s−s} and {s−s}, again the thin solid line.

Ag xz orbital, scheme 11. to play an important role. Calculations show that the xz orbitals are indeed more strongly effected by the adsorbate than other Ag d orbitals, based on a comparison of the dispersions of the projected DOS. Notwithstanding energy differences, xz crystal orbitals are able to interact with *all* of the O$_2$ orbitals, π as well as σ. The projected DOS of three important O$_2$ MO's $1\pi_u$, $3\sigma_g$ and $1\pi_g$ are provided in fig. 2. The $3\sigma_u$ O$_2$ orbital is too high in energy to interact effectively with the substrate. Note that the major peaks of the $1\pi_u$ and $3\sigma_g$ projections fall in essentially the same energy range. The projected DOS of the Ag xz orbital in scheme 5 is shown in the left panel of fig. 3. The dotted integration line indicates that some xz states move
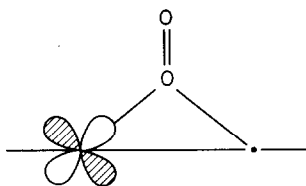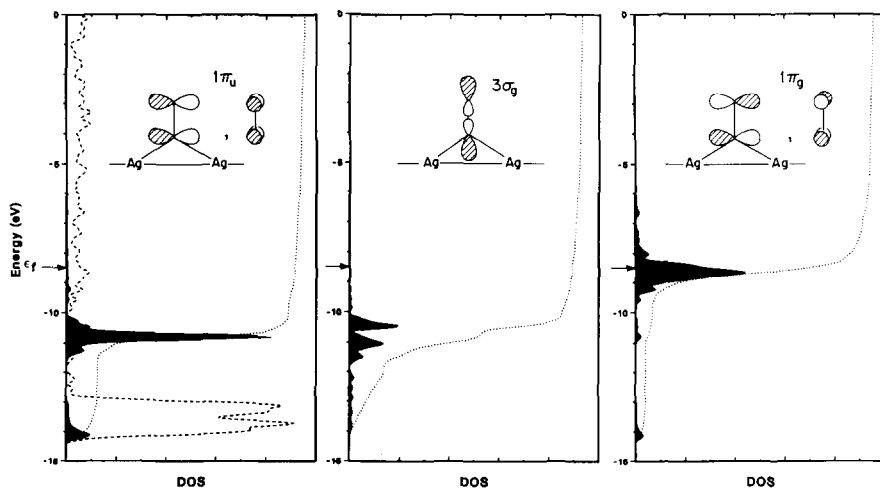

Scheme 11.

Fig. 2. Total DOS of scheme 5, bridging perpendicular 1.6 Å, dashed line. The projection DOS magnified $10\times$ (solid) and integrations (dotted) of the O_2 $1\pi_u$, $3\sigma_g$ and $1\pi_g$ levels in the left, center and right panels, respectively.

to the O_2 $3\sigma_g$, $1\pi_u$ and $1\pi_g$ regions. But these features are rather small, and not very convincing. Certainly it is difficult to differentiate between interactions with the $1\pi_u$ and $3\sigma_g$ levels. Approximately 90% of the xz levels remain in the Ag d block between -14.3 and -12.7 eV.
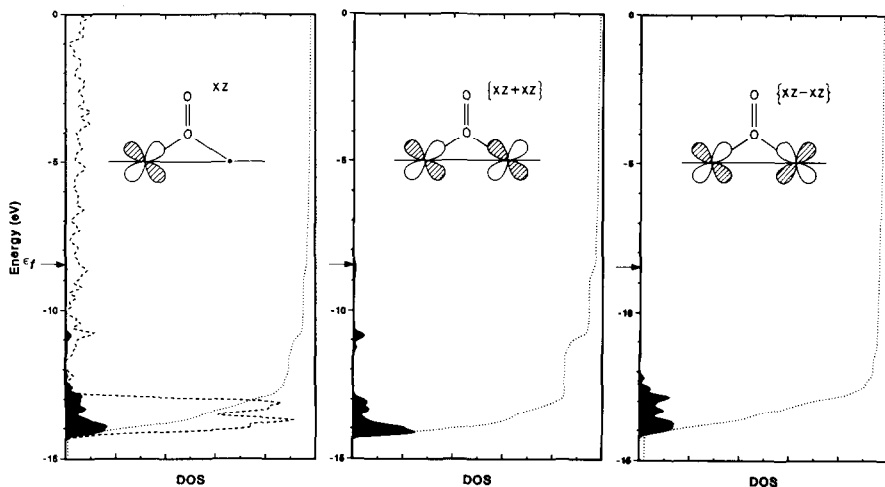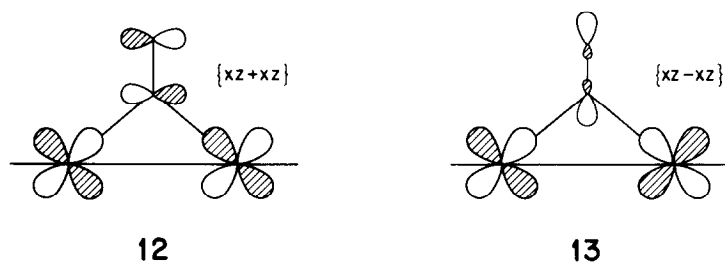

Fig. 3. Total DOS of scheme 5, bridging perpendicular 1.6 Å, dashed line. The projection DOS magnified $10\times$ (solid) and integrations (dotted) of the surface Ag xz atomic orbital, and the GODOS of the $\{xz + xz\}$ and $\{xz - xz\}$ group orbitals of bridged Ag_2 unit in the left, center and right panels, respectively.

$\{xz+xz\}$

$\{xz-xz\}$

12   **13**

Schemes 12 and 13.

However, we know that by symmetry a different set of crystal orbitals can interact with the O_2 π MO's than with the σ MO's. Those interacting with the π O_2 MO's must be Ag–Ag antibonding across the bridged atoms, $\{xz + xz\}$, scheme 12, whereas those interacting with the σ set must be Ag–Ag bonding, $\{xz - xz\}$, scheme 13. The GODOS of schemes 12 and 13 are depicted in the center and right-hand panels of fig. 3 respectively. The Ag–Ag bonding combination on the right shows, in fact, a very weak interaction with the O_2 $3\sigma_g$ orbital, as essentially no $\{xz - xz\}$ density is found in the main $3\sigma_g$ energy region between -10.0 and -12.0 eV. This is corroborated by the O_2 projections (fig. 2); if there were a strong interaction, some localization of $3\sigma_g$ density should be observed in the $\{xz - xz\}$ GODOS region. The O_2 $3\sigma_g$ density is spread more uniformly throughout the d block. The only obvious interaction of the bonding Ag xz orbitals with oxygen MO's comes from the
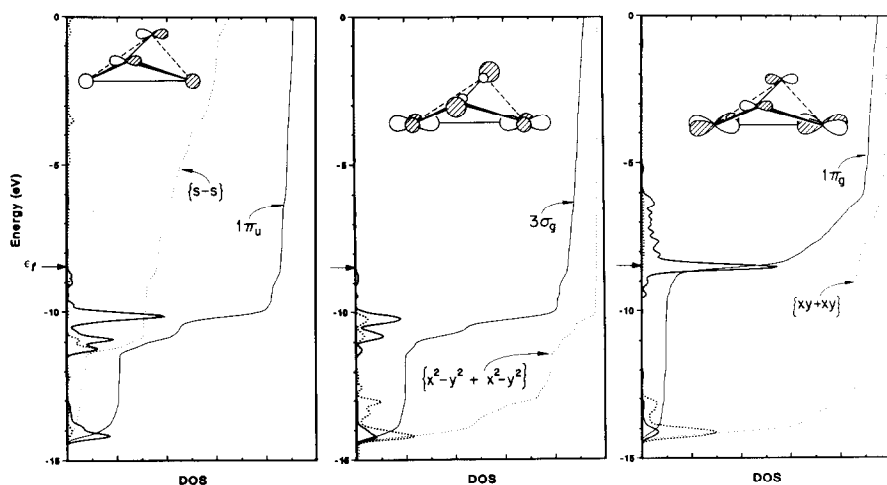

Fig. 4. Major interactions between O_2 orbitals (solid) and the group orbitals of the bridged Ag_2 unit (dotted) of scheme 3, bridging parallel. In the left panel, O_2 $1\pi_u$ and the Ag $\{s-s\}$ group orbital. In the center, O_2 $3\sigma_g$ and $\{x^2 - y^2 + x^2 - y^2\}$. On the right, O_2 $1\pi_g$ and $\{xy + xy\}$.

very low lying O_2 σ MO's, as can be observed in the nonzero value of the integration at the bottom of the energy window.

The integration of the GODOS of scheme 12 is in strong contrast, showing a well defined feature in the O_2 $1\pi_u$ region, near -10.9 eV, in particular and a smaller peak near ϵ_F, in the $1\pi_g$ region. The strong $1\pi_u-\{xz + xz\}$ interaction is verified by the concentration ($\sim 10\%$) of $1\pi_u$ states in the xz region of the Ag d block, at -14.0 eV. By comparing the three panels of fig. 3, the utility of the group orbital concept is evident. We can "presort" the crystal orbitals by the local symmetry of the site and eliminate combinations without the proper symmetry. The resultant projections will not be diluted by unimportant, less involved orbitals.

4. O_2 adsorption: bridging parallel

In the following sections we will discuss the binding characteristics of three of the seven O_2 binding sites in detail. As very little interaction can be seen in the two on-top sites, schemes 1 and 2, we begin with the bridging parallel geometry, scheme 3 at $d(\text{Ag–O}) = 1.6$ Å. In the three panels of fig. 4 are depicted the projected DOS of the $1\pi_u$, $3\sigma_g$ and $1\pi_g$ states (solid lines) and the GODOS of the group orbital of the Ag_2 unit (dotted lines) providing the strongest interaction in each case. This choice is based on a visual comparison of the projections; pairs are interacting if they have the proper symmetry and have very similar features in their DOS and integration curves. It is our experience that the integration curves, perhaps difficult to read at first, in the end turn out to be the easiest to follow visually while one tries to sort out which interactions are actually important. First, from the large dispersion observed in the O_2 projections, it is clear that the O_2–Ag interaction is strong at this site. In fact, as we will show in a later section, this particular site provides the strongest O_2–Ag interaction based on a variety of "yardsticks" that we have devised.

Both $1\pi_u$ and $3\sigma_g$ have large ($\sim 20\%$) peaks in the Ag d block. The $3\sigma_g$ levels mix with the bonding $x^2 - y^2$ group orbital as well as the bonding xz combination; since the xz bonding GODOS is essentially identical to that of $x^2 - y^2$, only the latter is shown in the figure. A complication arises in that Ag orbitals which interact with $3\sigma_g$ can, by symmetry, interact with one of the $1\pi_u$ orbitals as well. In addition, these orbitals are separated by only 1.0 eV in free O_2 so the $3\sigma-1\pi_u$ mixing will be very strong. However, if these projections are examined carefully, there are distinctions between the two. The $3\sigma_g$ projections have strong peaks *between* -10.0 and -11.0 eV, whereas the strongest $1\pi_u$ features occur *at* -10.0 and -11.0 eV. The previously mentioned xz and $x^2 - y^2$ bonding group orbitals more closely follow the $3\sigma_g$ pattern. In addition, we can project out the two $1\pi_u$ orbitals independently, and the one

which can mix with $3\sigma_g$, i.e. with the nodal plane parallel to the surface, is strongly localized ($\sim 60\%$) in the large peak at -10.0 eV in the figure, whereas the second, having a nodal plane perpendicular to the surface, is less strongly localized ($< 35\%$). None of the Ag group orbitals have strong features at -10.0 eV, thus the first $1\pi_u$ orbital is best described as non-bonding. The dispersion of the $1\pi_u$ projection is then due primarily to the second orbital, and its best Ag group-orbital match is the $\{s - s\}$ antibonding combination. Approximately 25% of this Ag state is localized in a peak near -11.0 eV; in comparison, no features in the $\{s + s\}$ bonding group orbital projection carry more than 8% of the total density. It is rather unusual to find such a strong metal s–adsorbate interaction [23]. Although the s orbitals are more diffuse, and for this reason may have a better overlap with the adsorbate MO's, they are generally dispersed over such a wide energy range that few states will have a good energy match with the adsorbate MO's.

The third panel of fig. 4 are the $1\pi_g$ O_2 and $\{xy + xy\}$ GODOS. In this case, the interaction is best discerned from the similarity of the integration curves. Because the energy difference between the Ag d levels and $1\pi_g$ is much greater than with $3\sigma_g$ and $1\pi_u$, the mixing will not be as strong. As with the $1\pi_u$ set, the $1\pi_g$ orbital with a nodal plane parallel to the surface is essentially non-bonding and localized in the sharp peak between -8.0 and -9.0 eV, slightly below ϵ_F. The total occupation of this level is $\sim 65\%$, thus some O–O bond weakening has occurred.
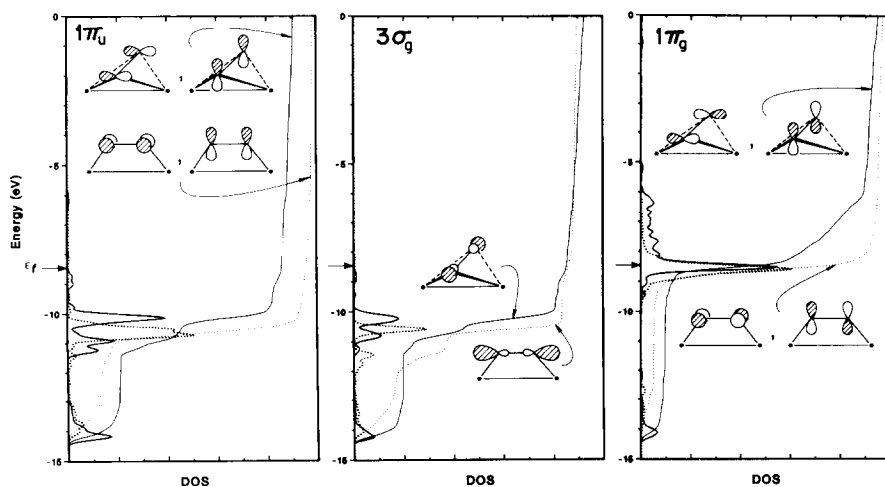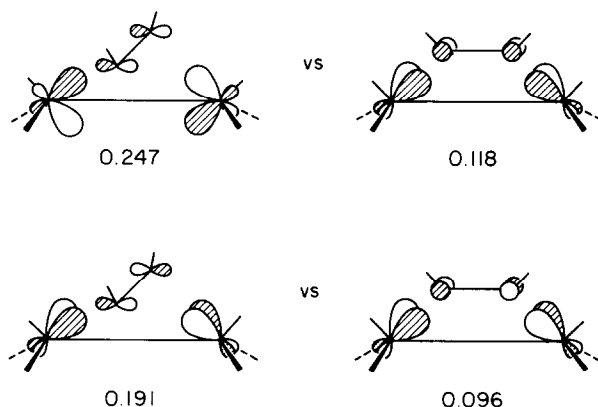

Fig. 5. Comparison of O_2 orbital projections and integrations for scheme 3, bridging parallel, with solid lines and scheme 4, di-σ bound, with dotted lines. The O_2 $1\pi_u$, $3\sigma_g$ and $1\pi_g$ levels are depicted in the left, center and right panels, respectively.

0.247   vs   0.118

0.191   vs   0.096

Scheme 14.

5. O$_2$ adsorption: di-σ

The di-σ site in scheme 4 is best discussed when contrasted to the bridging parallel site in scheme 3. The integrations of the $3\sigma_g$, $1\pi_u$ and $1\pi_g$ projected DOS of the two sites are given in fig. 5, as a solid line for scheme 3 and a dotted line for scheme 4. For each O$_2$ orbitals a higher percentage of the density is found in the Ag d block, near -14.0 eV, in the case of the bridging parallel mode. More states are pushed up above the median energy point for the π levels as well. The dispersion of the Ag group orbitals is weaker for scheme 4. All in all, the bridging parallel model is a much better candidate for the dissociation site than is the di-σ model. This finding is consistent with observations made about organometallic dimers bridged by acetylene [24]. Although both parallel and perpendicular L$_3$M(acetylene)ML$_3$ complexes coexist for the same metal d-electron count, the overlap between the metal dimer unit and the acetylene is more favorable for the perpendicular orientation. For the test complex Co$_2$(CO)$_6$(μ-C$_2$H$_2$), the two pairs of interactions showing the largest differences involve acetylene π orbitals with a node perpendicular to the metal plane. These are reproduced in scheme 14, along with the calculated overlaps.

6. O$_2$ adsorption: 3-fold hollow, perpendicular

When the O$_2$ is placed perpendicular to the surface in the 3-fold hollow site, with d(Ag–O) ≈ 1.6 Å, one oxygen atom lies in the Ag surface plane. Although this places it 2.36 Å away from the second layer Ag atom directly below, there is no indication of an interaction in the projected DOS of that Ag
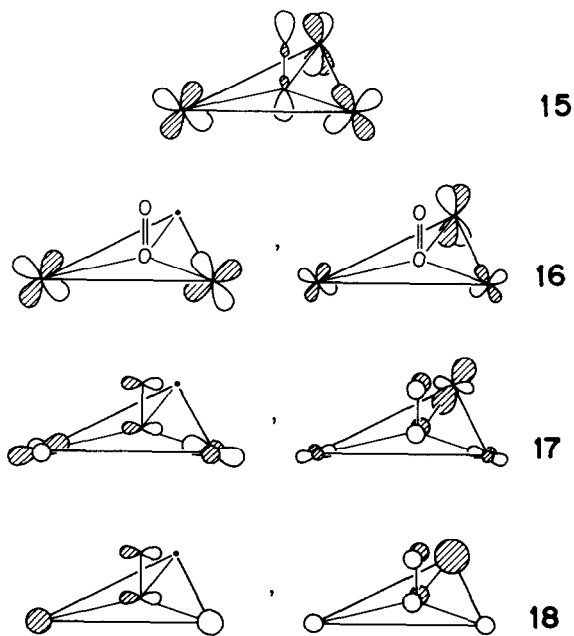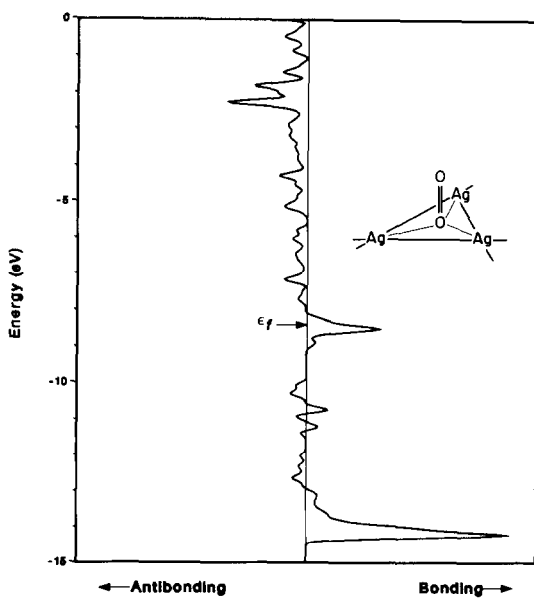
Schemes 15–18.

Fig. 6. COOP curve for Ag–O bound in scheme 7, 3-fold hollow perpendicular binding. The stong bonding peak falls in the Ag d block; the peak at ϵ_F is mainly $O_2 \, 1\pi_g$.

center. The characteristic binding of this site is best described using the group orbitals of Ag_3 unit in the first layer. Because one oxygen atom lies in the surface plane, Ag d orbitals having a node in this plane have the proper symmetry to mix with O_2 $3\sigma_g$, those without such a node can interact with $1\pi_u$ and $1\pi_g$. The strongest interaction with $3\sigma_g$ is observed in the radial metal d–π bonding group orbital, scheme 15. The degenerate antibonding combinations, scheme 16, are not involved in Ag–O bonding. The degenerate radial metal d–σ antibonding pair, scheme 17, and the antibonding Ag s pair, scheme 18, are most strongly mixing with O_2 $1\pi_u$ and somewhat less with $1\pi_g$. Rather than showing each projected DOS, many of these features can be recognized in the Ag–O COOP curve in fig. 6. As this curve is produced by weighting the total DOS by the contribution made to the Ag–O overlap population (o.p.) over some small energy range δE, the figure can help us to localize each of these interactions energetically. Most of the Ag–O bonding is derived from primarily Ag d states near -14.0 eV, as seen from the large positive peak at this energy. The $3\sigma_g$ and $1\pi_u$ regions cycle through bonding and antibonding peaks. There is a strong Ag–$1\pi_g$ feature directly below ϵ_F; the corresponding higher-lying antibonding levels are more diffuse. The total Ag–O o.p. is 0.50.

7. Comparison of O_2 sites on Ag(111)

Our main aim is to rate the O_2–Ag interaction of the seven sites, schemes 1–7, and to identify those state(s) most likely to lead to dissociation and those leading to charge transfer. Typically, one can follow the occupation of an antibonding MO, one that must be fully occupied for the desired reaction to proceed. In this case, it is $1\pi_u$, which is half occupied in free O_2. Because the $1\pi_u$ level lies 0.4 eV below ϵ_F of Ag(111), the reference point at infinite separation is O_2^{2-}, Ag(111)$^{2+}$. But we know that the oxygen molecule must acquire a negative charge as it approaches the surface. Thus this particular reference point is not useful for our analysis. A second choice is to raise the H_{ii} of the oxygen p orbital by 1.0 eV, so that $1\pi_g$ will fall above the Ag ϵ_F, and the reference becomes O_2^{2+}, Ag(111)$^{2-}$. Now difficulties arise at sites where the adsorbate–substrate interaction is minimal, for example the on-top perpendicular of scheme 2. The $1\pi_g$ interaction is predicted to be small at such a site, the $1\pi_g$ peak remains very peaked if d(Ag–O) = 1.6 Å (see panel 2, fig. 7). However, because of the mixing between the various O_2 MO's, some $1\pi_u$ and $3\sigma_g$ is pushed above ϵ_F, into the $1\pi_g$ peak. The net charge on the O_2 adsorbate becomes $+2.1$ e$^-$, an unreasonable result. A third option is to artificially assign a neutral charge to both adsorbate and substrate at infinite separation. However, the $D_{\infty h}$ symmetry of the O_2 molecule is broken by the presence of the silver slab, even at infinite separation. Thus mixing will occur between the $3\sigma_g$, $1\pi_u$ and $1\pi_g$ levels. The result is that the lower two will be depopulated at
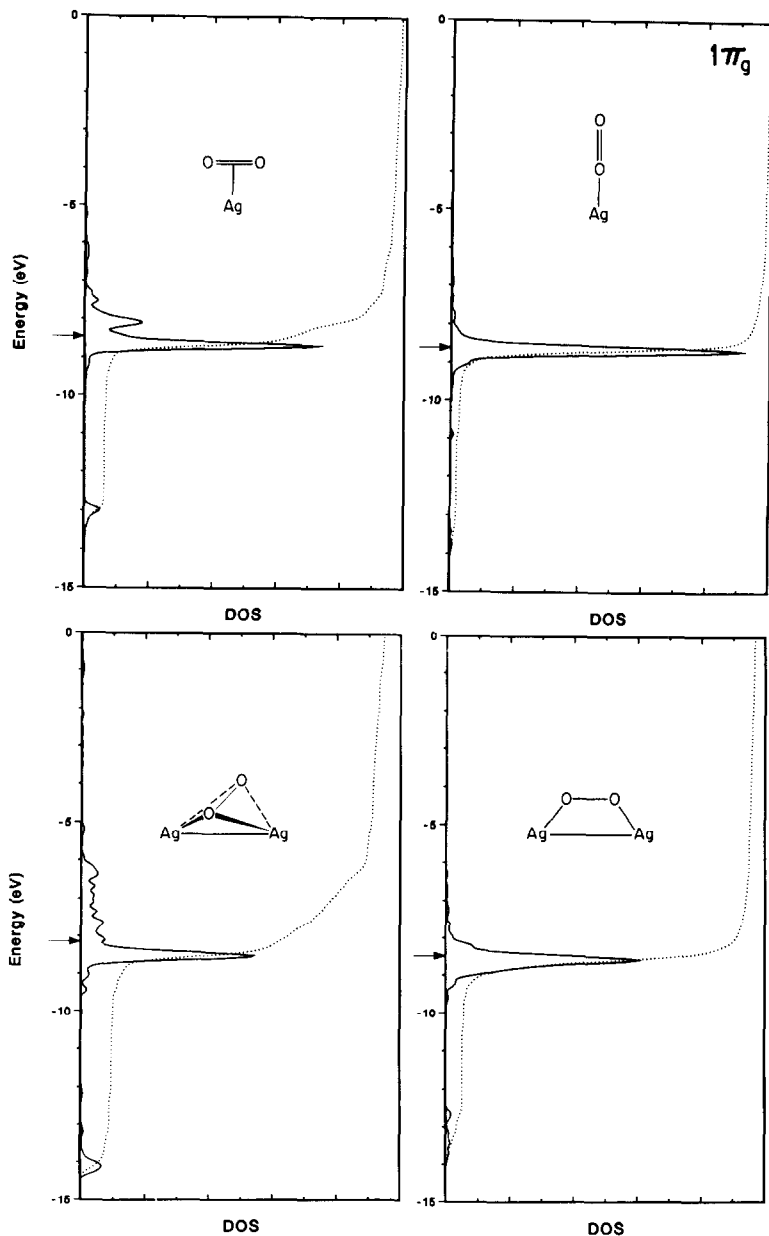
Fig. 7. The projected DOS magnified 10× and integration of the O_2 1π level, all with $d(Ag-O) = 1.6$ Å. On this page: scheme 1, on-top parallel, top left; scheme 2, on-top perpendicular, top right; scheme 3, bridging parallel, bottom left; scheme 4; di-σ, bottom right. On the next page: scheme 5, bridging perpendicular, top left; scheme 6, 3-fold hollow parallel, top right; scheme 7, 3-fold hollow perpendicular, bottom.

Fig. 7. Continued.

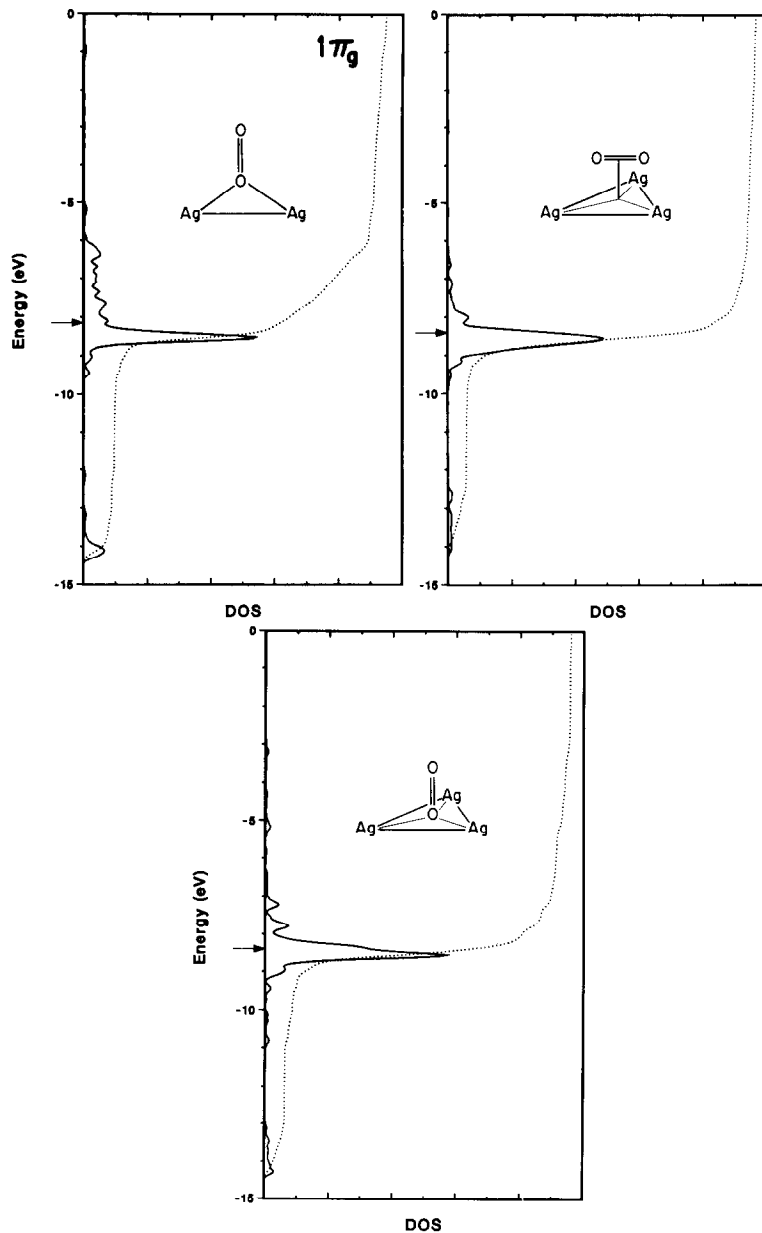a constant ϵ_F, and a fractional positive charge will develop on O_2. Although this may not cause a problem in the analysis, it should be taken into consideration.

Table 1
Comparison of Ag(111)–O_2 sites [a]

Scheme	Model	Ag–O distance (Å)	$1\pi_g$ occupation (%)	Charge on O_2
1	On-top parallel	1.6	70	− 0.54
		2.0	50?	+ 0.18
		2.5	97	+ 0.18
2	On-top perpendicular	1.6	50?	+ 0.42
		2.0	50?	+ 0.28
3	Bridging parallel	1.6	65	+ 0.24
		2.0	70	− 0.14
4	Di-sigma	1.6	70	+ 0.16
		2.0	70?	+ 0.93
5	Bridging perpendicular	1.6	70	− 0.22
		2.0	75?	− 0.56
6	3-fold parallel	1.6	70?	− 0.38
		2.0	75?	+ 0.18
7	3-fold perpendicular	1.6	70	+ 0.08
		2.0	70	− 0.32

[a] $1\pi_g$ occupations labeled with a "?" carry a ± 10% uncertainty; see text.

The last choice of reference point appears to be the best option. The $1\pi_g$ projected DOS of the seven sites at $d(\text{Ag–O}) = 1.6$ Å are collected in the two pages of fig. 7. Table 1 lists the percentage occupation of the $1\pi_g$ level and the total charge on O_2. In many cases, ϵ_F falls in the center of a sharp $1\pi_g$ peak, particularly if the Ag–$1\pi_g$ interaction is too weak to cause substantial dispersion of the peak. The $1\pi_g$ occupation becomes very dependent on the exact position of ϵ_F; unfortunately this makes the results sensitive to the particular number of layers chosen, or to the particular set of k points selected to represent the Brillouin zone. These entries are marked with a question mark. All in all, it is difficult to identify a pattern to the $1\pi_g$ occupations. Neither do the total O_2 charges follow any sort of rule. At 1.6 Å, the strongest electron transfer occurs to the model of scheme 1, on-top parallel, but at 2.0 Å to scheme 5, the bridging perpendicular mode. The bridging O_2 moieties all become more negative at longer distance. This is due to the strong mixing between $3\sigma_g$, $1\pi_u$ and $1\pi_g$, causing depopulation of the occupied O_2 MO's.

A more useful and reliable way to rank the Ag–O_2 interaction at the various sites is to measure the amount of dispersion induced in the $1\pi_g$ projected DOS directly. The greater the interaction, the more the dispersion. Regardless of whether we have chosen the proper parameters to obtain the correct ϵ_F and exact positions of the O_2 MO's relative to the Ag DOS, the relative extent of dispersion we calculate should be proportional to the ease of Ag → O_2 electron transfer.

Table 2
Calculating $1\pi_g$ dispersion [a]

Scheme	Model	Ag–O Distance (Å)	Method 1	Method 2	Method 3	m_2	$(m_2)^{1/2}$
1	On-top par	1.6	14	**40**	**8.1**	**0.429**	**0.655**
		2.0	5	10	0.9	0.124	0.352
		2.5	0	0	0.5	0.016	0.126
2	On-top perp	1.6	5	15	1.0	0.173	0.416
		2.0	0	0	0.9	0.034	0.184
3	Bridging par	1.6	**40**	**55**	**14.0**	**0.900**	**0.949**
		2.0	32	25	4.0	0.287	0.536
4	Di-σ	1.6	20	25	4.3	0.323	0.568
		2.0	18	25	3.0	0.288	0.537
5	Bridging perp	1.6	23	31	7.0	0.347	0.589
		2.0	18	27	4.2	0.284	0.533
6	3-fold par	1.6	22	25	6.1	0.394	0.628
		2.0	18	20	4.1	0.288	0.537
7	3-fold perp	1.6	18	**40**	**8.5**	**0.513**	**0.716**
		2.0	**30**	37	4.4	0.418	0.647

[a] Largest values are printed in bold face. Method 1 = ϵ_F lowered 0.5 eV $1\pi_g$ occupation; method 2 = percentage $1\pi_g$ outside 0.7 eV window; method 3 = ΔE containing 90% of $1\pi_g$.

"Dispersion" is a useful concept, easy so see at its extremes of being small or large, but difficult to assign one unique numerical definition. We have experimented with four different ways to gauge dispersion. Results from the four methods are compiled in table 2. First, to circumvent the problems stemming from the placement of ϵ_F in the center of the main $1\pi_g$ peak, ϵ_F was artificially lowered by 0.5 eV so as to fall below that peak. This particular energy was chosen because the observed width of a non-interacting peak, defined by the two-dimensional net of adsorbates alone, is approximately 0.7 eV. The non-zero width arises from interadsorbate interactions and the use of Gaussian functions to produce the DOS curves. The $1\pi_g$ occupation produced in this manner gives an indication of the amount of $1\pi_g$ density pulled down in energy by the substrate. From the listing in the first column, the most strongly interacting site is that of scheme 3, bridging parallel at 1.6 Å. Somewhat less are the same geometry at 2.0 Å and scheme 7, 3-fold hollow, perpendicular at 2.0 Å. The lowest values come from the two on-top geometries, schemes 1 and 2. One obvious drawback of this method is that it ignores any possible asymmetry in the $1\pi_g$ projection, which may be severe as there are many more Ag, as well as O_2, orbitals below than above.

In the second column we thus tabulate the percentage of the $1\pi_g$ density which falls outside of a 0.7 eV-wide window about the main peak. As this is the defined width of a non-interacting orbital, any density outside this window should results directly from the Ag–O_2 interaction. Again it is scheme 3 which

is found most interacting. Next is again one of the 3-fold hollow perpendicular geometries, but now the one with the shorter contact, as well as the on-top parallel, scheme 1, at 1.6 Å. The remaining on-top models form the least interacting set.

A more systematic method is to measure the energy width ΔE containing 90% of the $1\pi_g$ states, i.e. $\Delta E = (E$ at 95% integration) $- (E$ at 5% integration). These results should be less influenced by the smoothing function, and independent of some arbitrary and system-dependent definition of "non-interaction". The results are consistent with method #2, scheme 3 is strongest, and approximately tied for second are schemes 7 and 1, all at 1.6 Å. The other on-top systems are again least interacting.

The most rigorous way to measure the extent of dispersion is to use statistical methods designed to describe curve shape by, for example, computing the moments of the curve. The rth moment of a function $f(x)$ over the range x_1 to x_n about some point $\bar{x}$ is defined as:

$$m_r = \frac{n^{-1} \sum_{i=1}^{n} f(x_i)(x_i - \bar{x})^r}{\sum_{i=1}^{n} f(x_i)}. \tag{3}$$

If the range is continuous:

$$m_r = \frac{\int_{x_1}^{x_n} f(x)(x - \bar{x})^r \, dx}{\int_{x_1}^{x_n} f(x) \, dx}. \tag{4}$$

The first moment gives the average of the distribution of a curve. It is zero if the curve is perfectly symmetrical about $\bar{x}$ and $\bar{x}$ is chosen to be the mean of the curve. The second moment measures the average of the square of the deviation about $\bar{x}$. Higher moments weigh points far away from $\bar{x}$ more and more heavily. The second moment about the free O_1 $1\pi_g$ energy, $\bar{E} = -8.78$ eV, is most suited to the present needs. If the $1\pi_g$ projected DOS $\rho_a(E)$ is defined over n discrete points E_i in the energy window:

$$m_2 = \frac{\int \rho_a(E)(E - \bar{E})^2 \, dE}{\int \rho_a(E) \, dE}. \tag{5}$$

The computed second moments are listed in the final column of table 2. Again, it is the bridging parallel site which is found to disperse most widely. Second is the 3-fold hollow perpendicular mode, and following that, the on-top parallel coordination, all at 1.6 Å.

Importantly, the second moment of an adsorbate level projected DOS can be more formally related to the survival probability of an exiting negative ion. As previously mentioned, the survival probability is dependent on the likelyhood of back tunneling of an electron from O_2 to the surface. The tunneling probability of an electron from (or to) a discrete level $(1\pi_g)$ to a continuum of states (Ag surface) can be approximated by Fermi's golden rule. By assuming the appropriate form of the projected DOS, the second moment can very simply be related to the tunneling probability.

We first assume that the adsorbates serve as a pertubation to the bare substrate crystal orbitals. In the scheme developed by Muscat and Newns [25] to describe the chemisorption of atoms and molecules to surfaces, the projected DOS of the the adsorbate will be a Gaussian:

$$\rho_a(E) = \frac{1}{\pi\Gamma(E)} \exp\left(-\frac{(E-\bar{E})^2}{\Gamma(E)^2}\right),$$ (6)

where the level width $\Gamma_a(E)$ is given as:

$$\Gamma_a(E) = \pi\sum_k |\langle\phi_a|V|\phi_k\rangle|^2 \delta(E-E_k^0).$$ (7)

The level width $\Gamma_a(E)$ is proportional to the transition probability ω, according to Fermi's golden rule. In the weak chemisorption limit, $\Gamma(E)$ can be assumed to be independent of energy. In addition, the exponential term can be expanded about $\bar{E}$, and thus Muscat and Newns approximate eq. (6) by:

$$\rho_a(E) \approx \frac{1}{\pi}\frac{\Gamma(E)}{(E-\bar{E})^2+\Gamma^2},$$ (8)

which is the more familiar form of the projected DOS. Let us retain the Gaussian form; the second moment of the project DOS then becomes:

$$m_2 = \int_{-\infty}^{\infty}(E-\bar{E})^2\frac{1}{\pi\Gamma}\exp\left(-\frac{(E-\bar{E})^2}{\Gamma^2}\right)\,\mathrm{d}E.$$ (9)

Substitution of variables $x=(E-\bar{E})$ produces:

$$m_2 = \frac{2}{\pi\Gamma}\int_0^{\infty}x^2\exp\left(-\frac{x^2}{\Gamma^2}\right)\,\mathrm{d}x,$$ (10)

which reduces to:

$$m_2 = \Gamma^2/2\sqrt{\pi}.$$ (11)

Thus as Γ is proportional to the transition probability w:

$$w \propto \sqrt{m_2}.$$ (12)

If we assume a Gaussian form of the projected DOS, the transition probability is proportional to the square root of the second moment of the curve. These numbers are given in the final column of table 2. The larger the second moment, the greater the back-tunneling probability, and the lower the survival probability of the newly formed negative ion. In general, it is the hollow and bridged sites which have the largest second moments, and thus are least likely to produce negative ions. However, because the charge transfer to O_2 along the *incoming* trajectory is strongest at these sites, more dissociative products are expected to form.

8. Charge transfer: a comparison with experiment

In the previous sections we showed that the interaction of the O_2 $1\pi_g$ level with Ag is strongest at the bridge and hollow sites (see table 2). Similar results were obtained for the $1\pi_u$ and $3\sigma_g$ O_2 orbitals. In this section, we will use this result to explain the experimentally observed formation of O_2^- and O^- in the scattering of O_2^+ from Ag(111) [8,9].

The neutralization step ($O_2^+ \rightarrow O_2$) along the incoming trajectory has been described extensively elsewhere [9b]. O_2 molecules which survive the neutralization without dissociation, are converted into O_2^- ions close to the surface. This ion formation is the net result of the depletion of the bonding $1\pi_u$ and $3\sigma_g$ orbitals, and of the filling of the antibonding $1\pi_g$ orbital [9b]. The interaction of these orbitals with the silver surface leads to a weakening of the O–O bond, which can result in dissociation. Alternatively, the impact with the surface can induce a 'mechanical' dissociation [11–13]. From dissociated O_2 molecules, O atoms and O^- ions result. The O_2^- ions which survive the collision will partially neutralize, similarly for the O^- ions from dissociated O_2^-. We expect, however, that the neutralization probability of O^- to be *smaller* than that of O_2^-, due to the larger electron affinity of oxygen atoms.

Experimentally accessible is the $O^-/(O^- + O_2^-)$ ratio, which is not only a measure of the dissociation probability, but of the reneutralization probability as well, as the likelihood of neutralization of the two ions differs. If the Ag(111) surface were perfectly flat, both processes would only be dependent on the normal component of the incoming velocity (see eq. (1)). It was shown, however, that the O_2–Ag(111) potential is very corrugated [12,13,26,27]. For such a corrugated system, classical trajectory calculations indicate that with constant normal velocity, the probability for mechanical dissociation reaches a maximum for an incoming polar angle θ_i (with respect to the surface normal) of about $60°$ [13]. For larger θ_i, the dissociation probability decreases, to finally reach a constant asymptotic value at $\theta_i \geq 80°$. For example, at incoming energies of 200 eV ($\theta_i = 70°$) and 3000 eV ($\theta_i = 85°$) and approximately

equal normal velocities, the mechanical dissociation probabilities are computed to be 0.65 and 0.40, respectively.

The experimentally observed $O^-/(O^- + O_2^-)$ ratio also shows a pronounced dependence on the parallel component of the velocity. However, the trends are reverse to the computed 'mechanical-dissociation' trends. The experimental $O^-/(O^- + O_2^-)$ ratio *increases* rather than decreases with increasing incoming angle θ_i. For example, in the two above cases, the experimental ratios are 0.20 [8] and 0.80 [9], respectively. This difference between classical trajectory calculations and experiment could be explained by two factors: (1) a larger experimental dissociation probability at large θ_i due to covalent interactions between molecule and surface not taken into account in the classical trajectory calculations, and/or (2) an experimentally smaller O_2^- survival probability (i.e., without reneutralization) at large θ_i.

It has been previously pointed out that at very grazing incidence angles, only particles which have have been scattered from bridge or hollow sites can be detected [13]. This is due to shadowing of the top sites by surrounding Ag surface atoms. At less grazing angles, for example $\theta_i = 70°$, however, a considerable number of particles scattered from top sites can be observed. Thus, O_2 molecules with incidence angles around $\sim 85°$ will have, on the average, a stronger interaction with the silver surface than molecules incident near $70°$, due to the difference in the sites that are sampled. A stronger interaction for the more grazing incident molecules means that these molecules will experience a *larger* dissociation probability due to covalent interactions, but a *smaller* survival probability as molecular O_2^- ions. In such a way, we can explain that covalent interactions increase the $O^-/(O^- + O_2^-)$ ratio when going to more grazing incident angles. This increase can be stronger than the decrease expected from mechanical dissociation alone, thus explaining the experimental results.

9. Conclusion

Of the seven sites considered in this study, bridging and hollow sites are found least likely to give charge transfer products. At these sites, the interaction of the Ag affinity level $1\pi_g$ with the silver surface is strong, producing a high tunneling probability of the electron from the molecule back to the surface. On the other hand, O_2 dissociation is more likely than at on-top positions, as the initial charge transfer into the $1\pi_g$ level will weaken the O–O bond.

In addition to the interaction of the $1\pi_g$ states, one should also consider the depopulation of the O_2 $1\pi_u$ and $3\sigma_g$ levels. Generally, these orbitals will be strongly dispersed at sites which also show a strong Ag–$1\pi_g$ interaction. Their depopulation will enhance the possibility of O_2 dissociation. However, com-

plete O_2 dissociation must be accompanied by population of the high lying $3\sigma_u$ orbital (see scheme 8). Our choice of parameters places this level at $+6.3$ eV; much too high for effective interaction with the silver substrate. The density of silver states in this energy region is simply too low to provide such an interaction. However, in truth, as $1\pi_g$ becomes partially populated, the O–O bond will lengthen. The $3\sigma_u$ energy will consequently drop, and start to interact with the substrate. Thus, although our models do not allow for complete O_2 dissociation, we can consider the strengthening of the Ag–$1\pi_g$ interaction as a precursor to the O–O bond lengthening, the first step of the reaction.

Acknowledgements

References

[1] See for example: J.N.M. van Wunnik and J. Los, Phys. Scripta T6 (1983) 27;
    J.J.C. Geerlings, P.W. van Amersfoort, L.F.Tz. Kwakman, E.H.A. Granneman, J. Los and J.P. Gauyacq, Surface Sci. 157 (1985) 151;
    Yangsun Jo, A. Shultz, T.R. Shuler and J.W. Rabalais, J. Phys. Chem. 89 (1985) 2113;
    M.L. Yu, Phys. Rev. Letters 47 (1981) 151.
[2] R. Brako and D.M. Newns, Surface Sci. 108 (1981) 253.
[3] U. Imke, K.L. Snowdon and W. Heiland, Phys. Rev. B 34 (1986) 41, 48.
[4] H. Rechten, U. Imke, A. Namiki, K.J. Snowdon, P.H.F. Reijnen and A.W. Kleyn, to be published;
    U. Imke, P.J. van den Hoek and A.W. Kleyn, to be published.
[5] A. Danon and A. Amirav, Phys. Rev. Letters 61 (1988) 2961.
[6] J.W. Gadzuk and S. Holloway, J. Chem. Phys. 84 (1986) 3502.
[7] E. Kolodney, A. Amirav, R. Elber and R.B. Gerber, Chem. Phys. Letters 111 (1984) 366.
[8] Pan Haochang, T.C.M. Horn and A.W. Kleyn, Phys. Rev. Letters 57 (1986) 3035; J. Electron Spectrosc. Related Phenomena 45 (1987) 361.
[9] (a) P.H.F. Reijnen, P.J. van den Hoek, A.W. Kleyn, U. Imke and K.J. Snowdon, Surface Sci., submitted;
    (b) P.J. van den Hoek and E.J. Baerends, Surface Sci., in press;
    (c) P.J. van den Hoek, E.J. Baerends and R.A. van Santen, J. Phys. Chem., in press.

[10] R. Hoffmann, J. Chem. Phys. 39 (1963) 1397;
R. Hoffmann and W.M. Lipscomb, J. Chem. Phys. 36 (1962) 3179; 37 (1962) 2872;
J.H. Ammeter, H.-B. Bürgi, J.C. Thibeault and R. Hoffmann, J. Am. Chem. Soc. 100 (1987) 3686.

[11] M.C. Zonnevylle, R. Hoffmann and S. Harris, Surface Sci. 199 (1988) 320.

[12] P.J. van den Hoek, T.C.M. Horn and A.W. Kleyn, Surface Sci. 198 (1988) L335.

[13] P.J. van den Hoek and A.W. Kleyn, J. Chem. Phys., in press.

[14] (a) J. Silvestre and R. Hoffmann, Langmuir 1 (1985) 621;
(b) S. Komiya, T.A. Albright, R. Hoffmann and J. Kochi, J. Am. Chem. Soc. 99 (1977) 8440;
(c) S.-S. Sung and R. Hoffmann, J. Am. Chem. Soc. 107 (1985) 578;
(d) K. Tatsumi, R. Hoffmann, A. Yamamoto and J.K. Stille, Bull. Chem. Soc. Japan 54 (1981) 1857;
V.I. Baranovskii and A.B. Nikolskii, Teor. Eksperim. Khim. 3 (1967) 527.

[15] T.E. Felter, W.H. Weinberg, P.A. Zhdan and G.K. Borreskov, Surface Sci. 97 (1980) L313.

[16] V.L. Moruzzi, J.F. Janak and A.R. Williams, Calculated Electronic Properties of Metals (Pergamon Press, New York, 1978).

[17] R.C. Baetzold, J. Chem. Phys. 68 (1978) 555.

[18] As they stand, these parameters produce a completely unphysical 2.0 eV gap above the d block in the DOS of bulk Ag, and an unreasonably high Fermi energy ($\epsilon_F = -7.00$ eV).
(a) C.J. Ballhausen and H.B. Gray, Molecular Orbital Theory (Benjamin, New York, 1964) p. 120;
(b) O.P. Charkin, Russ. J. Inorg. Chem. (Engl. Trans.) 19 (1974) 1589.

[19] S.P. McGlynn, L.G. Vanquickenborne, M. Kinoshita and D.G. Caroll, Introduction to Applied Quantum Chemistry (Holt, Rinehart and Winston, New York, 1972) pp. 423–431.

[20] M. Ayyoob and M.S. Hegde, Surface Sci. 133 (1983) 516;
R.B. Grant and R.M. Lambert, J. Catalysis 92 (1985) 364;
C.T. Campbell and M.Z. Paffert, Surface Sci. 143 (1984) 517;
C.T. Campbell, Surface Sci. 157 (1985) 43.

[21] P.J. van den Hoek, unpublished results.

[22] R.A. van Santen, Progr. Surface Sci. 25 (1987) 253; Thermomol. Struct. 173 (1988) 157; J. Chem. Soc. Faraday Trans. 83 (1987) 1915.

[23] See for example, refs. [14a,14c] and J.-Y. Saillard and R. Hoffmann, J. Am. Chem. Soc. 106 (1984) 2006.

[24] D.M. Hoffmann, R. Hoffmann and C.R. Fisel, J. Am. Chem. Soc. 104 (1982) 3858.

[25] (a) J.P. Muscat and D.M. Newns, Progr. Surface Sci. 9 (1978) 1;
(b) D.M. Newns, Phys. Rev. 178 (1969) 1123;
(c) T.B. Grimley, in Proc. Int. School of Physics "Enrico Fermi", Dynamic Aspects of Surface Physics Course LVIII, Ed. F.O. Goodman, 1974;
(d) R.A. van Santen and E.J. Baerends, in: Theoretical Models of Chemical Bonding, Part 4, Ed. Z.B. Maksic (Springer, Berlin, to appear).

[26] M.E.M. Spruit, P.J. van den Hoek, E.W. Kuipers, F.H. Geuzebroek and A.W. Kleyn, Phys. Rev. B, in press; Surface Sci. 214 (1989) 591.

[27] P.H.F. Reijnen and A.W. Kleyn, to be published.